Applied Catalysis B: Environmental 314 (2022) 121520

Contents lists available at ScienceDirect

Applied Catalysis B: Environmental

journal homepage: www.elsevier.com/locate/apcatb

O_2 activation and $^1O_2$ generation over phosphate modified BiOCl for efficient photodegradation of organic pollutants

Hua Xu [a,*], Xiangming Liu [a], Hao Li [b,*], Lizhi Zhang [b]

[a] School of Chemistry and Environmental Engineering, Wuhan Institute of Technology, Wuhan 430205, China
[b] Key Laboratory of Pesticide & Chemical Biology of Ministry of Education, Institute of Environmental Chemistry, Central China Normal University, Wuhan 430079, China

ARTICLE INFO

Keywords:
Phosphate modification
O_2 activation
$^1O_2$ generation
BiOCl
Photocatalysis

ABSTRACT

Phosphate modification over semiconductor photocatalyst was an effective route to promote photodegradation of organic pollutants. Studies on promoted O_2 adsorption, better charge separation, and free •OH radicals raised from phosphate modification are clear, whereas O_2 activation and the generated reactive oxygen species ($\cdot O_2^-$, H_2O_2, and $^1O_2$) have been ignored. Herein, the hydrogen bond network constructed between BiOCl surface and phosphate weaken the surface Bi-O bond thus benefit the formation of oxygen vacancy (OVs). OVs not only facilitate the adsorption of organic pollutants but also promote the O_2 activation to generate H_2O_2 and $^1O_2$. Another route for $^1O_2$ generation relies on the H_2O_2 reacted with HClO from lattice chlorine oxidation was demonstrated. The directly attack of surface adsorbed 4-CP via h^+, in addition with the selective oxidation via $^1O_2$, synergetically contribute excellent photodegradation performance. This study systematically reveals the O_2 activation and $^1O_2$ generation for efficient photodegradation over phosphate modified BiOCl.

1. Introduction

Photodegradation of organic pollutants has emerged as one of the promising routes to convert persistent organic pollutants into more biologically degradable and less toxic substances [1,2]. Modification of semiconductor photocatalyst (e.g. TiO_2 [3–10], C_3N_4 [11,12] and BiOCl [13,14]) by inorganic nonmetal anions (such as PO_4^{3-}) was reported as a facile route to enhance the photocatalytic activity, since those anions could greatly influence the surface chemistry of semiconductors, thus accordingly change the photodegradation pathway of those organic pollutants via promoting the generation of certain reactive oxygen species (ROS) [15,16]. In particular, the generation of ROS, including hydroxyl radicals (•OH), superoxide radicals ($\cdot O_2^-$), hydrogen peroxide (H_2O_2), and singlet oxygen ($^1O_2$) are largely dependent on the surface chemistry and reaction environmental in the photocatalysis. After the modification of phosphate on either TiO_2 or BiOCl, more free •OH would be released for the more versatile reaction with surface bound/unbound organic substrates/intermediates; of which the phosphate either building the negative electronic field for the better charge separation over TiO_2 [3], or acting as brönsted acid/base sites for the formation of hydrogen bonds between H_2O and BiOCl surface to achieve better H_2O activation [14]. Additionally, the phenomenon of both the promoting O_2 adsorption and enhanced charge separation were observed on the phosphate modified photocatalysts [8–12]. O_2 as the ultimate oxidant could scavenge photogenerated electrons to generated ROSs, such as $\cdot O_2^-$ and H_2O_2. Nevertheless, it is noteworthy that, after the phosphate bounding with TiO_2, in spite of that a higher photodegradation efficiency resulting from the large amounts of free •OH is achieved, but the less H_2O_2 accumulation is observed, the further isotope-labeling analysis revealed that the free •OH which attack the benzoic acid is only from the oxidation of H_2O but not from the dissociation of H_2O_2 [5]. To date, the roles of negative electronic field and the favorable generation of free •OH is clearly, whereas seldom efforts is devoted on the O_2 activation for the production of ROS species ($\cdot O_2^-$, H_2O_2, and $^1O_2$) during the photodegradation over the phosphate modified photocatalysts.

Taking the bismuth oxychloride (BiOCl) as a prototypical model system, which owned a layered configuration characterized the stacking of [Cl-Bi-O-Bi-Cl] slices via the *van der Waals* interaction, usually crystalizes into nanosheets covered by (001) facet with exposure of O atoms on the top/bottom and (110) facet owned an open channel structure containing mobile lattice Cl on the four sides [17–19]. The surface modification of phosphate would construct a surface hydrogen bond network between the BiOCl surface and the phosphoric acid, thus selectively weaken the Bi-O bonds in a short range, which facilitate the

* Corresponding authors.
E-mail addresses: xu.hua@wit.edu.cn (H. Xu), backami@126.com (H. Li).

https://doi.org/10.1016/j.apcatb.2022.121520
Received 24 January 2022; Received in revised form 26 April 2022; Accepted 13 May 2022
Available online 16 May 2022

formation of surface oxygen vacancy (OVs) [20]. Oxygen vacancy is the most common and widely studied defect on metal oxides, localized by rich electrons of particular interest for enhanced O_2 activation [21–24]. Thus the O_2 activation is expected to be more promising after the phosphate modification of BiOCl. Besides the well-known reported $\bullet O_2^-$ ($O_2 + e^- \rightarrow \bullet O_2^-$) and O_2^{2-} ($\bullet O_2^- + e^- \rightarrow O_2^{2-}$ or $O_2 + 2e^- \rightarrow O_2^{2-}$), the formation of $^1O_2$, the excited state of triplet O_2, relies on either the direct energy transfer to O_2 [25–27], or the oxidation of $\bullet O_2^-$ to $^1O_2$ in the photocatalysis [28–30]. Moreover, H_2O_2 reacts with hypochlorous acid (HClO) will also yield stoichiometric amounts of $^1O_2$ via the formula $H_2O_2 + HClO \rightarrow {}^1O_2 + Cl^- + H_2O + H^+$ [32–36]. For the BiOCl, Shiraishi et al reported that the redox potential are 0.4–0.6, 1.23 and 1.36 V (vs. RHE) for the interlayer Cl^-/Cl_2, H_2O/O_2, and Cl^-/Cl_2, respectively. Therefore, the h^+ preferentially oxidize the interlayer Cl^- on the lateral (110) facets into active chlorine species and quickly yields the HClO in solution [37–40]. Finally, the HClO reacts with photogenerated H_2O_2 to produce $^1O_2$ and release Cl^- in the solution, the Cl^- in the solution could compensate the removed interlayer Cl^- for the Cl equilibrium. Benefits from the better charge separation, more h^+ would migrate from bulk to surface, thus the lattice chlorine oxidation over (110) facet and the produced HClO should be un-ignored for the phosphate modified BiOCl. To this end, we focus on the roles of phosphate modification of BiOCl on the O_2 activation and the involved generation of $^1O_2$.

The $^1O_2$ arisen from its unique $^1\Delta_g$ electronic configuration with a vacant π-antibonding orbital, which usually demonstrates ultrahigh selectivity for the oxidation of electron-rich moieties of aromatic substrates to yield the carbonyl (C═O) -containing intermediates, thus destabilize the conjugated-π system of the benzene ring for better ring-opening [41–43]. Meanwhile, the better charge separation resulted from the negative electronic field would drive more h^+ migrated to the BiOCl surface, the surface OVs could facilitate the adsorption of organic pollutants, thus those surface adsorbed substances would be directly attacked via the h^+. Herein, considering the high electrophilicity of $^1O_2$, two representative refractory pollutants, i.e., sulfamethazine (SMT) and 4-chlorophenol(4-CP), is well clarified based on comprehensive intermediates analysis. The structure-relationship among the O_2 activation, the origin of $^1O_2$, and the roles of ROS on the photodegradation of organic pollutant over phosphate modified BiOCl were systematically studied. This study provides an in-depth understanding on the O_2 activation and the related $^1O_2$ generation over phosphate modified BiOCl.

2. Experimental

2.1. Chemicals and materials

All analytical grade chemicals and materials were purchased from commercial suppliers and used without further purification.

2.2. Preparation of photocatalyst

In a typical procedure, 4 mmol of $Bi(NO_3)_3.5\,H_2O$ and 4 mmol of KCl were added in 50 mL of distilled water with continuous stirring for 30 min, then transferred to a 100 mL of Teflon-lined stainless autoclave and heated at 160 °C for 24 h. After hydrothermal treatment, the resulting precipitates were collected and washed with ethanol and deionized water thoroughly and dried at 60 °C in air. The sample was denoted as BOC.

For the phosphate modified BiOCl (denoted as P-BOC), 100 mg of above prepared BiOCl powder was dispersed into 100 mL of phosphoric acid solution (10 mg·L^{-1}) with continuous stirring in dark for 12 h. Then the suspension was centrifugated and washed with water thoroughly finally dried at 80 ℃ for 6 h.

2.3. Characterizations

The morphology was observed with a Hitachi S4800 field-emission scanning electron microscope (SEM) and JEOL JEM-2100 F transmission electron microscopy (TEM). X-ray photoelectron spectroscopy (XPS) tests were carried out by a Thermo ESCALAB 250XI spectrometer with an Mg Kα X-ray source, and the spectra calibrated to the C 1 s peak at 284.6 eV. The zeta potential was tested by a fully automatic potentiometric titrator (Metter Toledo T50). Fluorescence (PF) spectra were recorded on fluorescence spectrophotometer (Fluorolog-3, Horiba) at room temperature. Phosphorescence (PH) spectra were recorded on the Nanolog infrared fluorescence spectrometer (Nanolog FL3–2iHR, Horiba) at 77 K. The steady-state surface photovoltage (SS-SPV) spectra was collected by a lock-in amplier (SR830) synchronized with a light chopper (SR540). The mono-chromatic light was obtained by passing light from a 500 W xenon lamp (CHF-XM-500 W, perfectlight) through a double prism monochromator (Omni-λ300, Zolix). FTIR spectra was recorded by Nicolet iS50FT-IR spectrometer (Thermo) with a designed reaction cell. The surface oxygen vacancy and the reactive oxygen species were detected by the Electron spin resonance (ESR) instrument (A300–10, Bruker) at 77 K and (JES-FA300, JEOL) at room temperature, respectively. Free radicals (·OH and·O_2^-) and $^1O_2$ were detected by ESR using 5,5-dimethyl-1-pyrroline-N-oxide (DMPO) and 2,2,6,6-tetramethyl-4-piperidinol (TEMP) as trapping agents, respectively. The O_2 temperature-programmed desorption (O_2-TPD) curves were measured via Quantachrome ChemBET Pulsar. The concentration of ionic (including Cl^-, SO_4^{2-}, NH_4^+) were analyzed by ion chromatography (IC, Dionex Aquion RFIC, Thermo) with either anion or cation exchange chromatography column (Dionex IonPac™ AS23 or Dionex IonPac™ CS12A). The eluent was 4.5 mmol•L^{-1} $NaCO_3$ and 0.8 mmol•L^{-1} $NaHCO_3$ with a flow rate of 1.0 mL•min^{-1}.

2.4. Analytical method

Molecular oxygen activation measurements: 1 mg of catalyst was dispersed into 5 mL of 3,3′,5,5′-tetramethylbenzidine solution (TMB, 500 μM, HAc/NaAc buffer solution), then the mixture was illuminated with a 300 W Xenon arc lamp. The oxidation of TMB was evaluated by monitoring the absorbance around 380 nm with a UV–visible spectrophotometer (UV-2600, Shimadzu). Scavenger tests were carried out as the similar procedure mentioned-above but with certain amount of scavengers (isopropanol (IPA), 10 μL; superoxide dismutase (SOD), 6000 unit•mL^{-1}, 1 mg); catalase (CAT), 4000 unit•mL^{-1}, 5 μL; L-Histidine (L-His.), 10 mg.).

The concentration of H_2O_2 was measured via the N, N-diethyl-p-phenylenediamine sulfate (DPD)/peroxidase (POD) method. 50 mg of DPD was dissolved in 5 mL of 0.1 mol•L^{-1} H_2SO_4, denoted as DPD solution. 5 mg of POD was dissolved in 5 mL of deionized water, denoted as POD solution. 1 mL of sample solution was mixed with 0.05 mL of DPD solution, 0.05 mL of POD solution, and 1 mL of sodium phosphate buffer (0.1 mol•L^{-1}, pH=6.0). The concentration of H_2O_2 was determined by the absorbance at $\lambda = 551$ nm using the UV–visible spectrophotometer (UV-2600, Shimadzu).

The measurement of the concentration of hypochlorite (HClO): 1 mL of the sample solution was added in the mixture of 1 mL phosphate buffer (pH = 6.5) and 1 mL of above-mentioned DPD solution, and recorded the absorbance at $\lambda = 510$ nm using the UV–visible spectrophotometer (UV-2600, Shimadzu).

2.5. Photocatalytic degradation of pollutants

The photodegradation activity was evaluated by taking sulfamethazine (SMT) or 4-chlorophenol (4-CP) as two representative refractory pollutants under UV light irradiation ($\lambda > 300$ nm). 50 mL of aqueous suspension containing 10 mg•L^{-1} of SMT or 4-CP and 50 mg of catalysts was placed in a quartz glass beaker. The photoreaction was taken place in the open atmosphere without additional O_2 bubbled. Prior to irradiation, the suspension was magnetically stirred in dark for 30 min to get the adsorption-desorption equilibrium. A 300 W Xenon arc lamp (PLS-

SXE300 +/UV, Perfect Light, China) was utilized as light source (light intensity: 200 mW·cm^{-2}). Flow cooling water was employed outside the reaction beaker to control the reactor temperature ~ 10 °C. 1 mL of solution was sampled at predetermined time intervals of 5 min and filtered through a 0.22 μm polyethersulfone Millipore filter for analysis. The photocatalytic experiments were conducted in triplicate, with the results averaged in the analysis. The concentration of organic pollutants was detected by a high-performance liquid chromatograph (HPLC, U3000, Thermo), and the detection wavelength was fixed to be 263, 285, and 270 nm for SMT, 4-CP, and phenol, respectively. The total organic carbon (TOC) of the solution was tested by a combustion-type TOC analyzer (TOC-L, Shimadzu). The intermediates of SMT or 4-CP were analyzed from the gas chromatography-mass spectrum (GC-MS, TSQ Quantum MAX, Thermo).

In this study, the E-coli inactivation experiment was also carried out in the similar photoreaction system, and the inactivation activity was evaluated by counting the colonies number of viable bacteria after incubating the sample solution on nutrient agars at 37 °C for 20 h.

3. Results and discussion

3.1. Phosphate modification associated better charge separation

We firstly modified phosphate over BiOCl surface according to the previous reported method [20]. All characteristic diffraction peaks in both pristine BiOCl (BOC) and phosphate modified BiOCl (P-BOC) matched well with the tetragonal PbFCl-type BiOCl (JCPDS File no. 06–0249) (Fig. S1). As shown in Fig. 1a, HRTEM image of an individual nanosheet of P-BOC revealed lattice fringes of 0.275 nm that could be corresponded to the typical (110) plane of BiOCl. The corresponding SAED pattern was indexed as the [001] zone of tetragonal BiOCl, of which the angle between the displayed (110) and (200) planes is 45°, indicating that the BiOCl nanosheets were exposed with (001) facet on the top. Accordingly, the side surface is covered with (110) surface, which owned an open channel structure containing mobile lattice Cl. The corresponding elemental mapping images reveal the uniform distribution of Bi, O, Cl and P elements in P-BOC (Fig. S2). The strong peaks at 133.0 eV in P 2p XPS spectra of P-BOC can be assigned to the valence state of + 5 existing in the form of PO_4^{3-} (Fig. 1b). Then, the pH-zeta potential test revealed that the point of zero zeta potential (PZZP) is obviously shifted to lower pH value for the P-BOC suspension (Fig. 1c), indicating that the surface phosphate anions form a negative electrostatic field on the surface layer of P-BOC in aqueous suspension, which will drive more positive holes migrate from bulk to surface followed with a better charge separation.

As shown in Fig. 1d, the emission peak centered at 400 nm in the steady state PF spectra was assigned to the intrinsic band-edge emissions of BiOCl, it is noteworthy that P-BOC exhibited the lower PF intensity than that of BOC. The dynamic PF spectra (inset of Fig. 1d) further revealed that the lifetime of both BOC and P-BOC are the similar. The steady-state surface photovoltage (SS-SPV) spectroscopy is sensitive to study the photogenerated charge properties over nanosized semiconductor [44,45]. As shown in Fig. 1e, P-BOC exhibits much stronger SS-SPV response than that of BOC in the range of 300–370 nm, suggesting the better charge separation over P-BOC. The further electrochemical impedance spectra (Fig. S4) suggest that the P-BOC exhibited a semicircle arc with a smaller diameter thus assigned to the lower resistance value for electron-transfer, finally leading to 2 times higher of photocurrent density of P-BOC (29 μA·cm^{-2}) in compare with that of BOC (Fig. 1f). Those results indicating that P-BOC own the better charge separation ability than that of BOC, thus more charge carriers would migrate from bulk to surface, accordingly the h^+ would directly oxidize the adsorbed organic pollutants over surface active sites and the e^- could activate the adsorbed O_2 to generate reactive oxygen species.

3.2. Surface hydrogen bond resulted oxygen vacancy over P-BOC

The phosphate modification of BiOCl by using H_3PO_4 adsorbed on

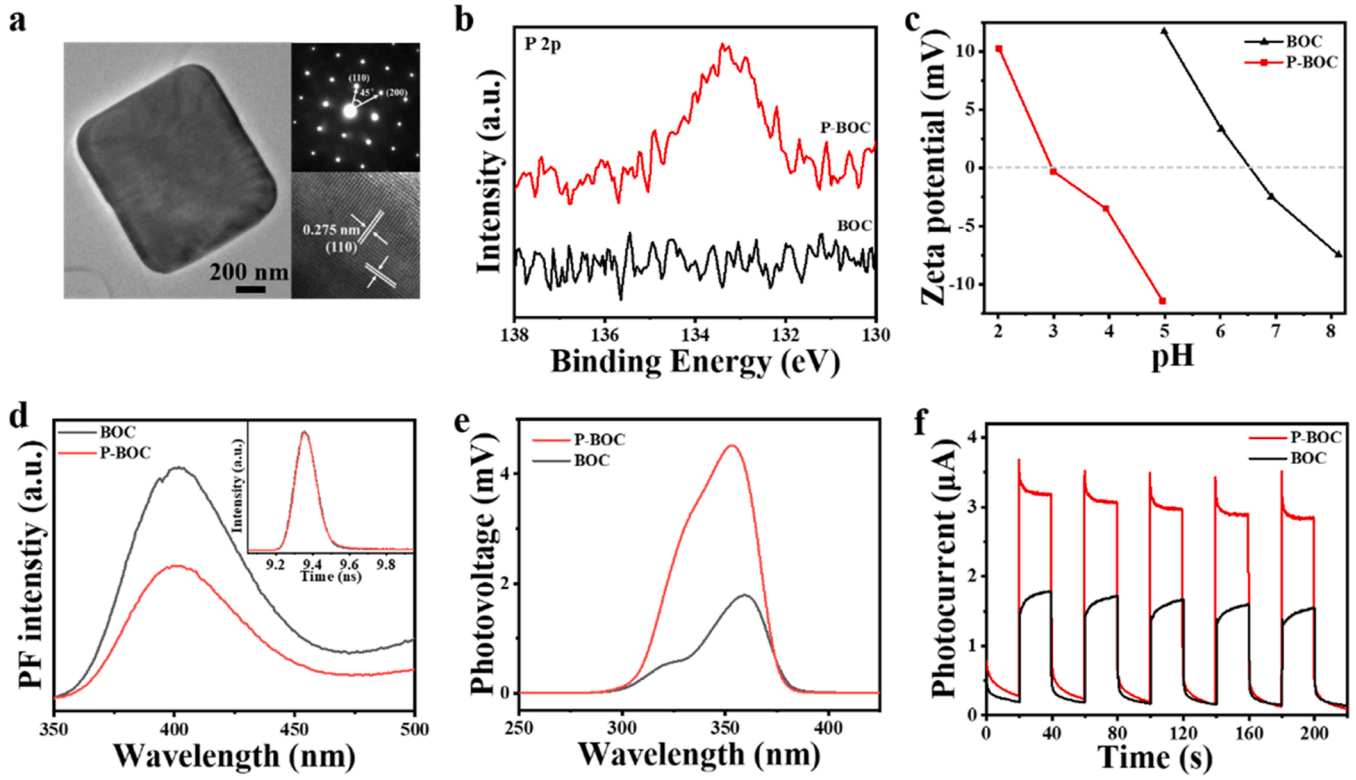

Fig. 1. (a) TEM and the related HRTEM images as well as SAED pattern of P-BOC, (b) XPS spectra of P2p, (c) pH-zeta potential relation curves, (d) steady state and dynamic (inset of d) fluorescence (PF) spectra recorded with 330 nm excitation, (e) steady state surface photovoltage spectra, (f) photocurrent I-t curves.

BiOCl surface through weak hydrogen bonds could weaken the surface Bi-O bond and thus facilitate the formation and regeneration of surface oxygen vacancy (OVs) under light illumination over P-BOC surface. As shown in Fig. 2a, the ATR-FTIR spectra revealed that, the -OH stretching band of H_3PO_4 at 3000–3500 cm^{-1} gradually shifted to a lower wavenumber and the matching deformation band at approximately 1635 cm^{-1} slightly shifted to a higher wavenumber after the adsorption of H_3PO_4 over BiOCl, while other P═O and P═O-H stretching vibrations exhibited salient absorptions in the fingerprint region (1003, 1075, and 1173 cm^{-1}), substantiated the existence of the interfacial hydrogen bonds network between the -OH of H_3PO_4 with the O-Bi of BiOCl [20]. In compare with pristine BOC, the Bi 4 $f_{5/2}$ and Bi 4 $f_{7/2}$ bands lower-shifted by 0.4 eV for P-BOC (Fig. 2b), which are ascribed to the weakening of the Bi-O bond induced by the surface hydrogen bond after phosphate modification. Then, the in-situ ESR spectra of both BOC and P-BOC powders before and after light illumination were recorded at low temperature of 77 K. As shown in Fig. 2c, the signal centered at $g = 2.002$, which correspond to the surface oxygen vacancy, was much stronger for P-BOC than that of BOC. The further light illumination on the BiOCl powders via a high-voltage mercury lamp makes the signal grow a lot over P-BOC, indicating that much more OVs existed and re-generated over P-BOC. Raman spectra, being sensitive to the short-range lattice distortion, were used to further study the structural difference and validate the regeneration of oxygen vacancy under light irradiation. As shown in Fig. S5a, the representative vibration bands with the frequencies centered at 61, 146 and 202 cm^{-1} for BiOCl only shifted a little for BOC; whereas those bands obviously blue-shifted to 59, 142 and 198 cm^{-1} for P-BOC, which was aroused from the weaken Bi-O bond. Moreover, a new peak at 101.5 cm^{-1} assigned to the regenerated oxygen vacancy was appeared for P-BOC [23], of which the intensity linearly increased with the elongation of illumination time (Fig. S5b). Those experimental results well confirmed that the phosphate modification over BiOCl via constructing the surface hydrogen bond network would benefit for the formation and regeneration of oxygen vacancy through the selective Bi-O bond elongation.

The surface OVs could facilitate the O_2 adsorption, the adsorbed O_2 over BiOCl could capture the photogenerated e^- thus to prevent the accumulation of negative charges for promoted charge separation as well as to generate more reactive oxygen species in the photoreaction. As shown in Fig. 2d, the O_2-TPD curves revealed that the O_2 adsorption is weak over BOC, while the peaks appeared at ~376 and ~510 °C could be assigned to the chemical sorption of O_2 over P-BOC. It is noteworthy that a strong peak centered at 580 °C was observed, to exclude the possible decomposition of P-BOC, TG-DSC curves were further recorded. As shown in Fig. S6 , there was no mass change and obvious heat change during the heating process from room temperature to 700 °C. Thus, we can confirm that the peak centered at 580 °C for P-BOC is assigned to the chemical adsorption of O_2. Finally, the total amounts of O_2 adsorbed are measured to be 2.6 and 19.7 $\mu mol \cdot g^{-1}$ for BOC and P-BOC, respectively.

3.3. The roles of oxygen vacancy on the O_2 activation over P-BOC

Oxygen vacancy as the common anion defects over BiOCl play important roles on the O_2 activation during the photodegradation of organic pollutants. Using 3,3′,5,5′-tetramethylbenzidine (TMB) as the probe molecule, we evaluated the O_2 activation ability of both BOC and P-BOC in aqueous solution [46,47]. As shown in Fig. 3a, the absorbance evolution at 380 nm indicating the oxidation of TMB with ROS generated via O_2 activation over P-BOC. In compare with BOC, much more TMB was oxidized by P-BOC (Fig. 3b), indicating that P-BOC own much stronger ability on the molecular O_2 activation. Then, various ROS scavengers, such as isopropanol (IPA), superoxide dismutase (SOD), catalase (CAT), and L-Histidine (L-His.), were adopted to study the involved ROS for the TMB oxidation over P-BOC. As shown in Fig. 3c,

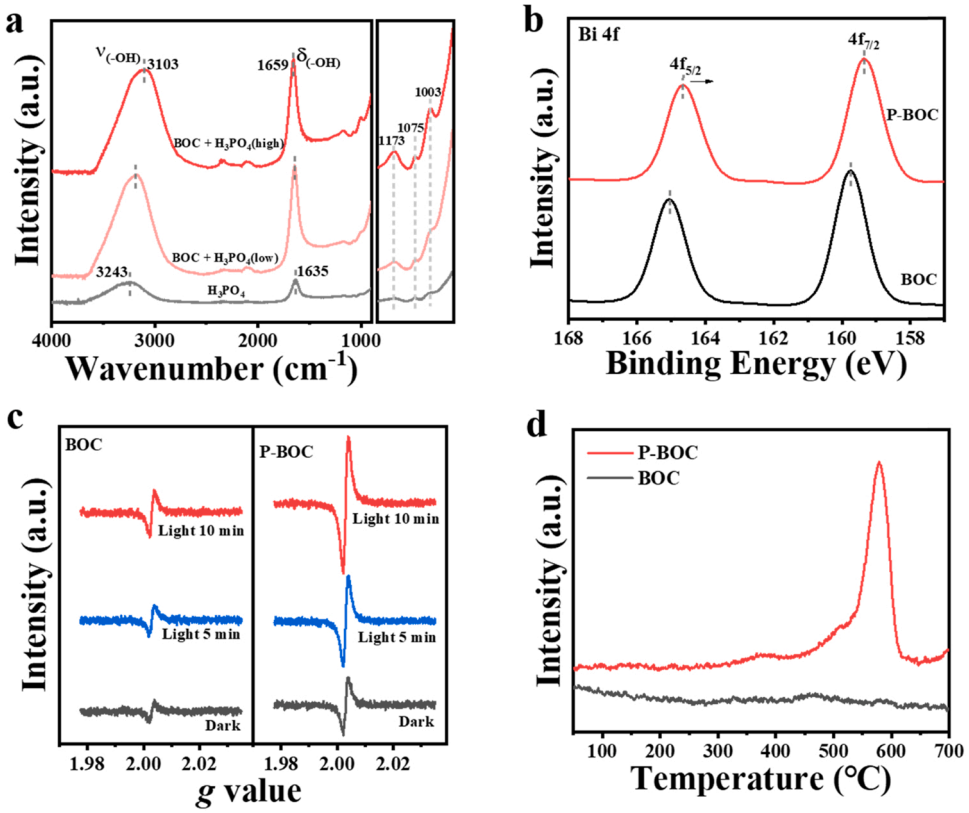

Fig. 2. (a) ATR-FTIR spectra of H_3PO_4 (300 mg•L^{-1}) and BiOCl dipped with low and high concentration of H_3PO_4 solution, (b) XPS spectra of Bi 4 f, (c) *In situ* ESR spectra of both BOC and P-BOC powders after 5 or 10 min of light irradiation in the sample tube and the spectra were recorded at 77 K, (d) O_2-TPD curves of BOC and P-BOC powders.

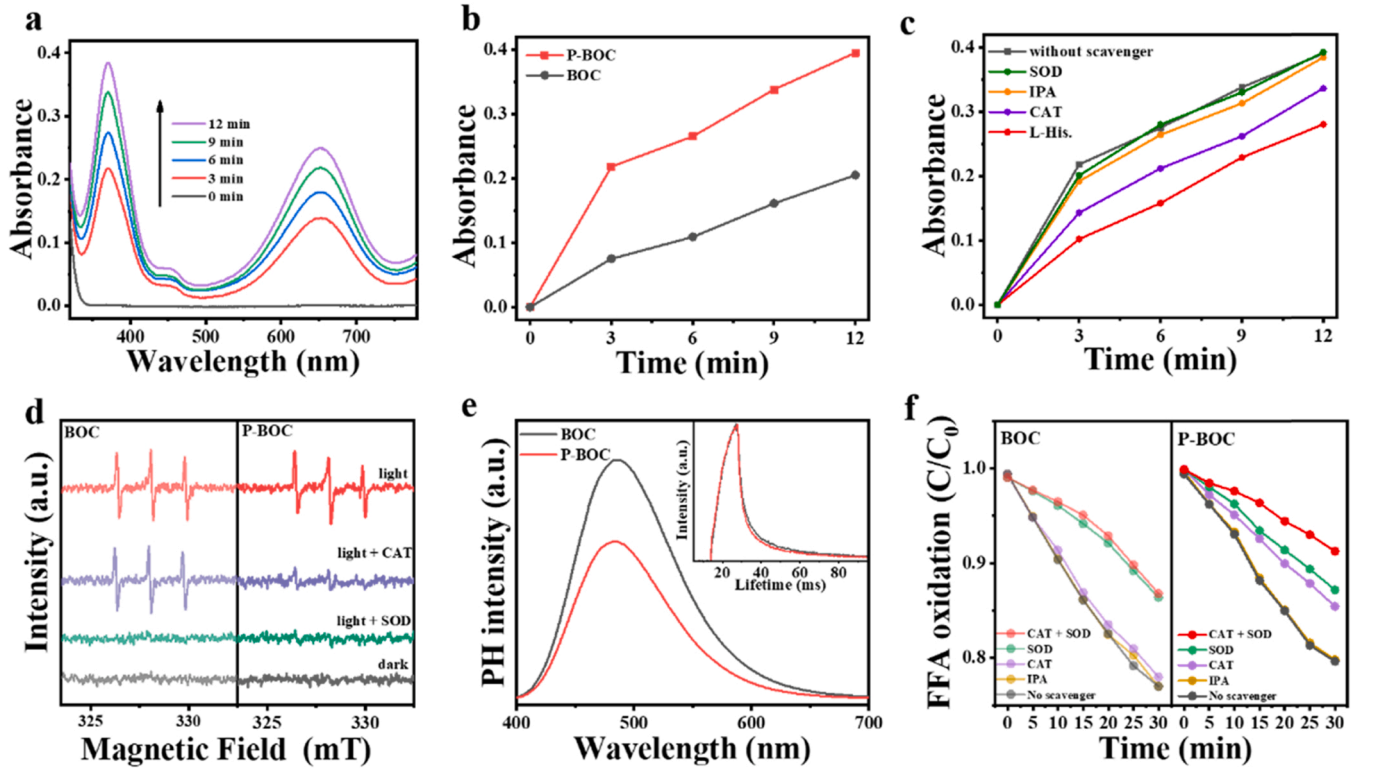

Fig. 3. (a) Time-dependent absorbance spectra of TMB oxidation over P-BOC under light illumination, (b) the absorbance evolution of TMB oxidation at the peak around 380 nm for both BOC and P-BOC, (c) the absorbance evolution of TMB oxidation at the peak around 380 nm over P-BOC in the presence of various scavengers, and (d) ESR spectra of the TEMP-$^1O_2$ adduct recorded in dark or without/with SOD and CAT under light illumination for 6 min over both BOC and P-BOC. (e) Phosphorescence (PH) spectra at 77 K (delay time of 5 ms) and the time-resolved PH spectra (inset) monitored at the emission peak of 485 nm. (e) $^1O_2$ evolution rates tested with various ROS scavengers added via furfuryl alcohol (FFA) as probe molecular.

both L-Histidine and catalase could largely suppress the TMB oxidation over P-BOC, indicating that $^1O_2$ and H_2O_2 are the major photogenerated ROS via O_2 activation over P-BOC.

Next, the reactive oxygen species were studied via the ESR spectra. Fig. S7a represent the ESR signal of TEMP-$\bullet O_2^-$, of which much stronger ESR intensity was observed over BOC; the further quantitative analysis of $\bullet O_2^-$ via nitroblue tetrazolium (NBT) as probe molecular also suggest that more $\bullet O_2^-$ could be detected over BOC than that of P-BOC (Fig. S7b). As shown in Fig. 3d, no signal could be observed in dark but a typical 1:1:1 triplet signal indexed to the TEMP-$^1O_2$ adduct could be obviously detected upon light illumination for both BOC and P-POC. In particular, the control experiment results presented that, the addition of $\bullet O_2^-$ scavenger SOD in the photoreaction system retarding the formation of $^1O_2$ for BOC, either $\bullet O_2^-$ scavenger SOD or $^1O_2$ scavenger CAT could suppress the generation of $^1O_2$ over P-BOC, indicating that the route for the $^1O_2$ generation is obviously different over P-BOC from that over BOC. Both $\bullet O_2^-$ and H_2O_2 play important roles on the $^1O_2$ generation over P-BOC.

It is generally accepted that the $^1O_2$ generation in photocatalysis relies on two routes: the energy transfer process involving the spin-triplet excitons to overcome the spin-flip restrictions and the charge transfer process by oxidation of $\bullet O_2^-$. Firstly, the excitonic effect (electron-hole pairs bound by the attractive Coulomb interactions) existed in the confined layered semiconductors (such as BiOCl) allows for the generation of $^1O_2$. To check the excitonic effects in BiOCl, the phosphorescence (PH) spectra were recorded under 77 K with a decay time of 5 ms. The phosphorescence is induced by radiative decay from spin-forbidden excitonic states with a much longer lifetime thus could be distinguished from the PF spectra with a certain delay time. As shown in Fig. 3e, when the excitation light was fixed at 330 nm, different from the emission peak at 400 nm in the PF spectra, both BOC and P-BOC exhibits the strong PH emission peak at 485 nm, suggesting the existence of long-lived excitons in BiOCl. However, the PH intensity of P-BOC is less than that of BOC, which is in well-accordance with the PF spectra, since more charge carriers (e^-, h^+) separated and migrated to the P-BOC surface. The time-resolved PH spectra further presents that the lifetime of the excitonics in BOC and P-BOC are 121.7 and 112.9 ms, respectively (inset of Fig. 3e). The above-mentioned analysis suggesting that excitonic effect is existed in BiOCl and less $^1O_2$ would be released via the possible energy-transfer route over P-BOC in compare with BOC.

Another route for the $^1O_2$ generation from $\bullet O_2^-$ via charge transfer route is known in the previous report and listed as follows: $\bullet O_2^- + h^+ \rightarrow {}^1O_2$, $\bullet O_2^- + H_2O_2 \rightarrow {}^1O_2 + OH^- + \cdot OH$, $\bullet O_2^- + \cdot OH \rightarrow {}^1O_2 + OH^-$ [48]. To further quantitatively check the origin of $^1O_2$, furfuryl alcohol (FFA), which exhibits high reaction rate constants of $^1O_2$ equals to $k = 1.2 \times 10^8\ M^{-1}\cdot s^{-1}$, was used as the probe molecular [49]. As shown in Fig. 3f and Fig. S8, the addition of SOD could inhibit the selective FFA oxidation via $^1O_2$ over both BOC and P-BOC, while H_2O_2 scavenger CAT changed little over BOC but suppress the FFA oxidation over P-BOC. The phenomenon that the co-addition of SOD and CAT further decrease the FFA oxidation in compare with that either SOD or CAT solely added over P-BOC, ruling out the possible route for the $^1O_2$ generation via $\bullet O_2^- + H_2O_2 \rightarrow {}^1O_2 + OH^- + \cdot OH$. So there must be other contribution of H_2O_2 on the $^1O_2$ generation, which is unclear in photocatalysis.

3.4. $^1O_2$ generation from H_2O_2 reacted with HClO over P-BOC

It is widely accepted that hypochlorite ions (ClO^-) can react with H_2O_2 in solution to produce $^1O_2$ ($H_2O_2 + ClO^- \rightarrow {}^1O_2 + Cl^- + H_2O$) [31–36]. Then, we measured the concentration of Cl^- released over BiOCl in dark or under light illumination. As shown in Fig. 4a, much less Cl^- is dissolved in dark for P-BOC (6.6 μmol•L^{-1}) than that of BOC (25.4

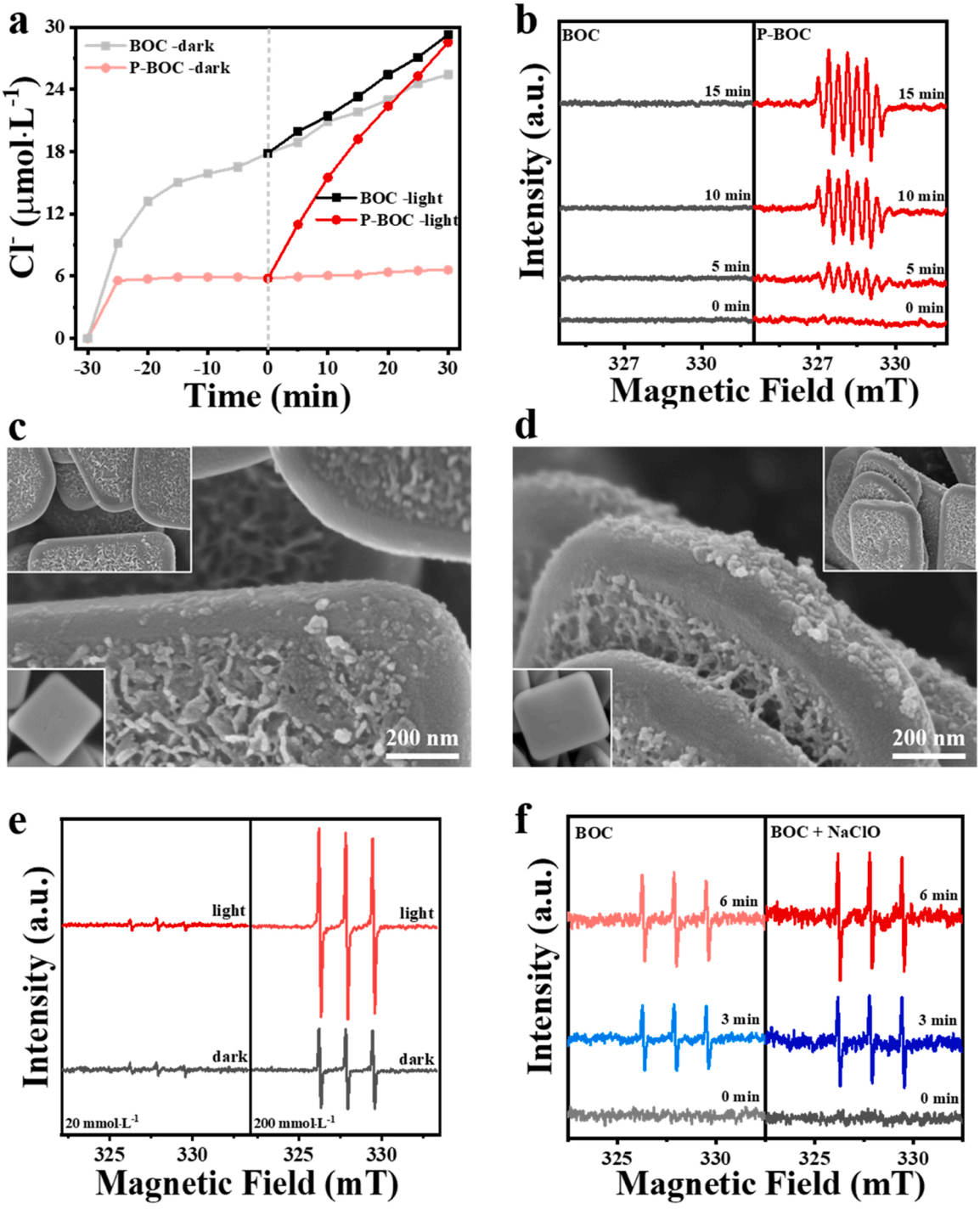

Fig. 4. (a) Concentration of Cl^- detected in the BOC and P-BOC suspensions in dark or under light illumination, (b) ESR spectra of DMPOX over BOC and P-BOC under light illumination, SEM images of BOC (c) and P-BOC (d) nanosheets before (inset in bottom) and after photodeposition of MnO_x nanoparticles, (e) ESR spectra of the TEMP-$^1O_2$ recorded in the mixture of H_2O_2 and HClO with different concentrations in dark or under light illumination for 6 min, (f) ESR spectra of the TEMP-$^1O_2$ recorded over BOC with the extra addition of NaClO (200 mmol•L^{-1}) in the solution under light illumination.

μmol•L^{-1}) due to the surface phosphate protection. However, the concentration of Cl^- dramatically and linearly increased upon light illumination and reached to 28.5 μmol•L^{-1} over P-BOC, since the better charge separation would push more h^+ migrated from bulk to surface thus trigger the lattice chlorine oxidation ($Cl^- + h^+ \rightarrow$•Cl, 2·Cl + $H_2O \rightarrow$ HOCl + Cl^- + H^+) over P-BOC. This explanation is further evidenced by the ESR spectra as shown in Fig. 4b. The seven-line ESR spectra of DMPOX, which is identified as the oxidized derivative of DMPO via the free active chlorine·Cl oxidation [50,51], was only detected in the P-BOC photoreaction system, and the intensity of this seven-line DMPOX linearly increased with the elongation of light illumination. The further SEM images (Fig. 4c-d) revealed that more MnO_x particles photodeposited on the (110) surface of P-BOC than that of BOC, since much more h^+ migrated to the P-BOC surface. Herein, the prepared BiOCl consisted of (001) facet on the top/bottom and (110) facet on the four sides. The (001) surface is rich with the hydroxyl group thus facilitate the building of hydrogen bond network with H_3PO_4, thus more surface OVs is favored to be generated on the (001) surface. Meanwhile, due to

the open channel structure exposing with Cl on the (110) surface, so the lattice chlorine oxidation is more easily occur on the side (110) facet. More h^+ driven from bulk to surface would result in more HClO production over P-BOC.

Considering the HClO might existed in the photoreaction system from the lattice chlorine oxidation, we can speculate that the coexistence of H_2O_2 and HClO would release the $^1O_2$ over P-BOC. The two-electron oxidation of H_2O_2 by HClO yielding the initial formation of $^1O_2$ based on the rate law $d[^1O_2]/dt = k_1$ [HClO][H^+][Cl^-] or $d[^1O_2]/dt = k_2$ [H_2O_2][ClO^-], and the formation rate largely dependent on the concentration of [HClO] or [ClO^-] [31]. As shown in Fig. 4e, the H_2O_2 and HClO mixture with different concentrations (20 mmol•L^{-1} vs 200 mmol•L^{-1}) were recorded via ESR to check whether $^1O_2$ would be released in dark or under light irradiation. ESR spectra confirmed that the intensity of the TEMP-$^1O_2$ signal is relevant to both the concentration of H_2O_2/HClO and the light illumination on/off, more $^1O_2$ would be generated with a higher concentration of H_2O_2/HClO, and the light illumination further promote this reaction. More powerful proof evidenced that the extra addition of NaClO (200 mmol•L^{-1}) in the BiOCl photoreaction system could promote the $^1O_2$ generation (Fig. 4f). Therefore, we can conclude that, the other reliable route for the $^1O_2$ generation over P-BOC relies on the oxidation of H_2O_2 by HClO (H_2O_2 + HClO→ $^1O_2$ + Cl^- + H_2O + H^+).

The band structures of the BiOCl samples were studied to check the redox potential of photogenerated e^- and h^+. As shown in Fig. S9a, the light absorbance edges were measured to be 366 and 368 nm for BOC and P-BOC, respectively. By plotting the light absorbance spectra using the Tauc plot formular, the band gaps of BOC and P-BOC are calculated to be 3.31 and 3.28 eV, respectively (inset of Fig. S9a). The flat band potentials of BOC and P-BOC from the Mott-schottky plots are respectively tested to be − 0.44 and − 0.41 V (Fig. S9b), indicating those catalyst could thermal dynamically activate O_2 for the ROS generation. Moreover, the ultraviolet photoelectron spectra (UPS) showed that the maximum valence band potentials of BOC and P-BOC are similar and recorded to be 2.75 eV (Fig. S9c). The reported redox potential of interlayer Cl^-/Cl_2 is ~ 0.4–0.6 eV (vs. RHE), lower than that of H_2O/O_2, thus the h^+ on the valence band of BiOCl prefer to oxidize the interlayer Cl^-. Once the lattice chlorine oxidized via h^+, after series of reaction (Cl^- + h^+ →•Cl, 2·Cl + H_2O → HOCl + Cl^- + H^+), the produced HClO would react with the photogenerated H_2O_2 to release $^1O_2$ and Cl^- in the photoreaction (H_2O_2 + HClO→ $^1O_2$ + Cl^- + H_2O + H^+). Those released Cl^- might go back to the BiOCl and complete the extraction/insertion cycle.

3.5. Photodegradation of organic pollutants

$^1O_2$ exhibited promising high selectivity to attack organic pollutants with electron-rich moieties, which would destabilize the benzene ring thus facilitate the ring-opening reaction. We then selected the SMT and 4-CP as target organic pollutants, which have been demonstrated refractory in the environment [52,53]. As shown in Fig. 5a-b, the self-degradation of SMT and 4-CP is negligible under light irradiation, while more than 90% of SMT and 4-CP could be photodegraded by P-BOC in 15 min, with the pseudo-first-order kinetics rate constants (k) calculated to be 0.27 and 0.16 min^{-1}, about 6 and 7.1 times of BOC, respectively. Next, various scavengers were added to investigate the contribution of those active species on the photodegradation. As shown in Fig. 5c-d, both •O_2^- and h^+ play important roles on the 4-CP and SMT photodegradation over BOC; while the $^1O_2$ instead of •O_2^- make great contribution on the photodegradation over P-BOC.

Then, the intermediates during the 4-CP photodegradation were systematically analyzed to study the reaction pathway. As shown in Fig. S10, p-benzenediol and 4-chlorobenzene-1,3-diol, in addition with other ring-opening products, were detected as the intermediates over BOC. For BOC, the •O_2^- directly attack the aromatic ring and remove a single Cl^- as the first key step to form p-benzenediol, or the attacking of •OH on the aromatic ring of 4-CP would generate the 4-chlorobenzene-1,3-diol. However, besides h^+, the $^1O_2$ acted as the predominant ROS species on the 4-CP photodegradation over P-BOC. It is interesting to find that, besides the p-benzoquinone and the small carboxylic acids, 6-cyclohexanone was detected in the GC-MS spectra for P-BOC; and the control experiment showed that the addition of $^1O_2$ scavenger L-Histidine could complete suppress the formation of 6-cyclohexanone and p-benzoquinone (Figs. S11 and 12). It is reported that $^1O_2$ could selectively oxidize the electron-rich moiety and destabilize the stubborn conjugated-π system to yield the C═O group contained products. The weaken of the conjugated-π system delivers the possibility in cleaving the benzene rings and thus leading to the higher photodegradation efficiency.

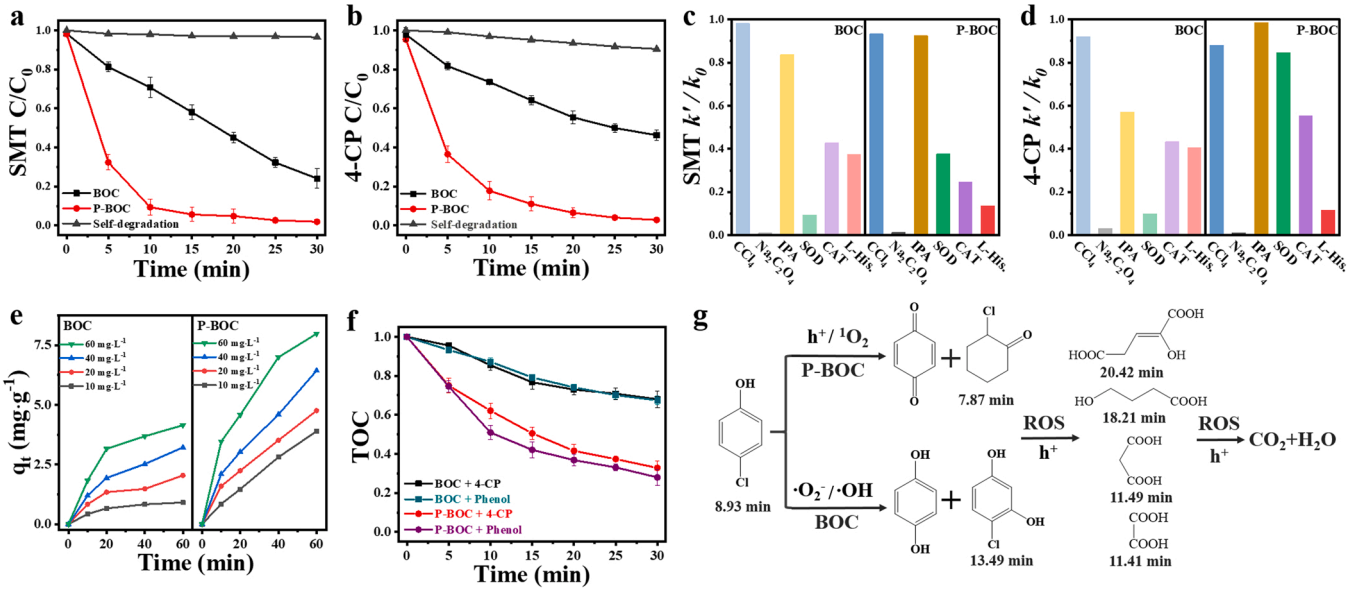

Fig. 5. Photocatalytic degradation curves of SMT (a) and 4-CP (b), the reactivity inhibition in the presence of various scavengers in the photodegradation of SMT (c) and 4-CP (d) over BOC and P-BOC under light illumination, (e) adsorption kinetic curves of 4-CP over 200 mg of BOC and P-BOC at room temperature, the concentration of 4-CP was ranged from 10 to 60 mg· L^{-1}, (f) TOC removal efficiency of 4-CP and phenol over BOC and P-BOC, and (g) the schematic illustration of the 4-CP photodegradation process over BOC and P-BOC based on the detected intermediates via HPLC and GCMS.

Moreover, the photogenerated h^+ with strong oxidization ability could directly oxidize the organic pollutants adsorbed over semiconductor surface. Previous study reported that the complexation of Bi on Bi_2O_3 with empty orbitals and Cl of 2-CP with lone-pair electrons could result in the stronger adsorption of 2-CP, thus leading to the direct h^+-induced pathway, in which h^+ could firstly activate then cleave the stable C-Cl bond [54]. Herein, even with phosphate modification, in compare with other semiconductor metal oxides photocatalyst, the Bi-O bond in BiOCl is more easily tuned for the generation of surface OVs. Surface OVs can not only benefit for the O_2 adsorption/activation but also good for the adsorption of organic pollutants. As shown in Fig. 5e, the adsorption kinetic curves of 4-CP revealed that more 4-CP molecular adsorbed over P-BOC due to the more surface OVs existed. Considering more h^+ migrated to the P-BOC surface because of the better charge separation, the direct oxidation of 4-CP via the strong oxidative h^+ would achieve a relatively high total organic carbon (TOC) removal efficiency. As shown in Fig. 5f, the TOC removal efficiency of 4-CP over P-BOC is 67.9% in 30 min, about 3.3 times of that of BOC (20.2%). Additionally, phenol with the similar molecular structure to 4-CP except the existence of Cl, was adopted to check the generality of the high TOC removal efficiency (Fig. S13). As shown in Fig. 5f, the TOC removal efficiency of phenol over P-BOC is high up to 72% in 30 min. Based on the intermediates detected by the high performance liquid chromatography (HPLC) and chromatography–mass spectroscopy (GC-MS), we draw the schematic illustration of the 4-CP photodegradation pathway over BOC and P-BOC as illustrated in Fig. 5g.

3.6. Quantitative analysis of the H_2O_2 and HClO for the $^1O_2$ generation

Furthermore, we systematically analyzed the concentration of both H_2O_2 and HClO along with the photodegradation of organic pollutants, to further study the generation of $^1O_2$ via the reaction of H_2O_2 and HClO ($H_2O_2 + HClO \rightarrow {}^1O_2 + Cl^- + H_2O + H^+$). During the photodegradation of organic pollutants (4-CP, phenol), due to the better charge separation, more h^+ migrated from bulk to surface thus the lattice chlorine oxidation is more, resulted in more HClO released over P-BOC. As shown in Fig. 6, the concentration of HClO in BOC raised to ~ 2 μmol·L^{-1} in the first few minutes then kept in constant, while the detected HClO increased and kept in ~ 10 μmol·L^{-1} in the last 15 min over P-BOC. The detected solution is in a volume of 50 mL, indicating that the HClO in the solution is less than 0.5 μmmol, those low concentration indicating that HClO reacted quickly with the produced H_2O_2 over P-BOC. This conclusion is further verified by the concentration curves of H_2O_2. Even the H_2O_2 is proven to be one of the O_2 activation products over P-BOC, the concentration of H_2O_2 is only slightly increased at first but almost kept in constant at ~ 20 μmol·L^{-1} (equals to 1 μmol in total) later; while the H_2O_2 continuously generated along with the reaction time and reached to ~ 110 μmol·L^{-1} in 30 min. The low concentration of H_2O_2 over P-BOC (~20 μmol•L^{-1}) might be ascribed to two aspects: the better photodissociation ability of H_2O_2 into ·OH (Fig. S16), and the reaction of H_2O_2 with HClO to generate $^1O_2$. In order to further evidence the origin of HClO arisen from lattice chlorine oxidation, 5 mg·L^{-1} of NaCl was extra added in the photoreaction system. Interestingly, for both BOC and P-BOC, the concentration of HClO is similar regardless of whether extra Cl^- added (Fig. S16), suggesting that the extra added Cl^- could not be oxidized into HClO. Moreover, since the addition of NaClO in H_2O_2 solution would generate $^1O_2$, and the extra addition of NaClO in the BOC photoreaction system could increase the TEMPO-$^1O_2$ signal, we extra added 500 μmol·L^{-1} of NaClO (instead of the lattice chlorine oxidation) in the BOC photoreaction system, it is noteworthy that the 4-CP degradation activity was ~2 times improved and the catalyst exhibited good stability in 4 cycles (Fig. S17).

Finally, we also investigate the roles of $^1O_2$ over P-BOC on the E-coli inactivation. As shown in Fig. S18, ~2.8 $\log_{10}$ of E-coli was self-inactivated under light irradiation ($\lambda > 300$ nm). P-BOC exhibits slightly higher E-coli inactivation efficiency than that of BOC, about

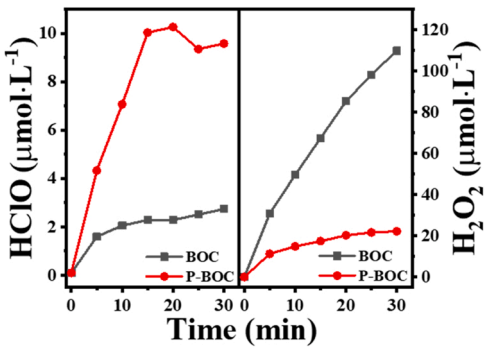

Fig. 6. Concentration of HClO and H_2O_2 detected during the 4-CP photodegradation over BOC and P-BOC.

~5.2 $\log_{10}$ of E-coli was inactivated over P-BOC. The $^1O_2$ trapping experiments revealed that the addition of $^1O_2$ scavenger L-Histidine largely suppress the inactivation efficiency over P-BOC, while almost no change occur over BOC, indicating that the E-coli inactivation pathway are obviously different over BOC and P-BOC. Previous study reported that the $^1O_2$ attack the proteins and phospholipids then diffuse into the cell to interrupt the bacterial energy metabolism and finally degrade the cell debris thus destruct the E-coli cell [55]. Both the organic pollutant photodegradation and E-coli inactivation experiment revealed that $^1O_2$ contribute greatly over the phosphate modified BiOCl.

4. Conclusion

In conclusion, we systematically studied the O_2 activation and $^1O_2$ generation as well as the photodegradation of organic pollutants over the phosphate modified BiOCl. The better charge separation resulting from the negative electronic field by PO_4^{3-} ions could drive more charge carriers (e^--h^+) migrated from bulk to surface. The more easily generated surface oxygen vacancy due to the weakened Bi-O bond would be benefit for the O_2 adsorption/activation and the adsorption of organic pollutants. The selective attacking of electron-rich moieties in aromatic substances via $^1O_2$ and the directly strong oxidation of organic pollutants via h^+ synergetically contribute the excellent photodegradation and TOC removal efficiency over P-BOC. Moreover, the h^+ could also oxidize the lattice chlorine oxidation to release HClO which reacts with H_2O_2 to generate $^1O_2$. This study enables us to gain the comprehensive understanding on the O_2 activation and $^1O_2$ generation over phosphate modified semiconductor photocatalyst.

Credit authorship contribution statement

Hua Xu: Methodology, Validation, Formal analysis, Writing, Project administration. **Xiangming Liu**: Investigation, Validation, Formal analysis. **Hao Li**: Methodology, Formal analysis. **Lizhi Zhang**: Conceptualization, Supervision.

Declaration of Competing Interest

The authors declare that they have no known competing financial interests or personal relationships that could have appeared to influence the work reported in this paper.

Acknowledgements

This work was financially supported by the Science Foundation of Wuhan Institute of Technology (Grant Number K201962).

Declaration of Competing Interest

The authors report no declarations of interest.

Appendix A. Supporting information

Supplementary data associated with this article can be found in the online version at doi:10.1016/j.apcatb.2022.121520.

References

[1] H. Li, J. Li, Z. Ai, F. Jia, L. Zhang, Oxygen vacancy-mediated photocatalysis of BiOCl: reactivity, selectivity, and perspectives, Angew. Chem. Int. Ed. 57 (2018) 122–138.

[2] H. Li, Z. Ai, L. Zhang, Surface structure-dependent photocatalytic O2 activation for pollutant removal with bismuth oxyhalides, Chem. Commun. 56 (2020) 15282–15296.

[3] D. Zhao, C. Chen, Y. Wang, H. Ji, W. Ma, L. Zang, J. Zhao, Surface modification of TiO2 by phosphate: effect on photocatalytic activity and mechanism implication, J. Phys. Chem. C. 112 (2008) 5993–6001.

[4] A. Bachinger, G. Kickelbick, Photocatalytic stability of organic phosphonates and phosphates on TiO2 nanoparticles, Appl. Catal. A: Gen. 409–410 (2011) 122–132.

[5] H. Sheng, H. Ji, W. Ma, C. Chen, J. Zhao, Direct four-electron reduction of O2 to H2O on TiO2 surfaces by pendant proton relay, Angew. Chem. Int. Ed. 52 (2013) 9686–9690.

[6] H. Sheng, H. Zhang, W. Song, H. Ji, W. Ma, C. Chen, J. Zhao, Activation of water in titanium dioxide photocatalysis by formation of surface hydrogen bonds: an in situ IR spectroscopy study, Angew. Chem. Int. Ed. 54 (2015) 5905–5909.

[7] Z. Wang, A. Mahmood, X. Xie, X. Wang, H. Qiu, J. Sun, Surface adsorption configurations of H3PO4 modified TiO2 and its influence on the photodegradation intermediates of gaseous o-xylene, Chem. Eng. J. 393 (2020), 124723.

[8] Y. Cao, L. Jing, X. Shi, Y. Luan, J.R. Durrant, J. Tang, H. Fu, Enhanced photocatalytic activity of nc-TiO2 by promoting photogenerated electrons captured by the adsorbed oxygen, Phys. Chem. Chem. Phys. 14 (2012) 8530–8536.

[9] L. Jing, X. Qin, Y. Luan, Y. Qu, M. Xie, Synthesis of efficient TiO2-based photocatalysts by phosphate surface modification and the activity-enhanced mechanisms, Appl. Surf. Sci. 258 (2012) 3340–3349.

[10] L. Jing, J. Zhou, J.R. Durrant, J. Tang, D. Liu, H. Fu, Dynamics of photogenerated charges in the phosphate modified TiO2 and the enhanced activity for photoelectrochemical water splitting, Energy Environ. Sci. 5 (2012) 6552–6558.

[11] C. Liu, L. Jing, L. He, Y. Luan, C. Li, Phosphate-modified graphitic C3N4 as efficient photocatalyst for degrading colorless pollutants by promoting O2 adsorption, Chem. Commun. 50 (2014) 1999–2001.

[12] Z. Li, Y. Luan, Y. Qu, L. Jing, Modification strategies with inorganic acids for efficient photocatalysts by promoting the adsorption of O2, ACS Appl. Mater. Interfaces 7 (2015) 22727–22740.

[13] Z. Li, Y. Qu, K. Hu, M. Humayun, S. Chen, L. Jing, Improved photoelectrocatalytic activities of BiOCl with high stability for water oxidation and MO degradation by coupling RGO and modifying phosphate groups to prolong carrier lifetime, Appl. Catal. B: Environ. 203 (2017) 355–362.

[14] L. Ding, M. Li, Y. Zhao, H. Zhang, J. Shang, J. Zhong, H. Sheng, C. Chen, J. Zhao, The vital role of surface Brönsted acid/base sites for the photocatalytic formation of free·OH radicals, Appl. Catal. B: Environ. 266 (2020), 118634.

[15] W. Sun, Q. Meng, L. Jing, D. Liu, Y. Cao, Facile synthesis of surface-modified nanosized α-Fe2O3 as efficient visible photocatalysts and mechanism insight, J. Phys. Chem. C. 117 (2013) 1358–1365.

[16] J. Wang, S. Wang, Effect of inorganic anions on the performance of advanced oxidation processes for degradation of organic contaminants, Chem. Eng. J. 411 (2021), 128392.

[17] J. Jiang, K. Zhao, X. Xiao, L. Zhang, Synthesis and facet-dependent photoreactivity of BiOCl single-crystalline nanosheets, J. Am. Chem. Society134 (2012) 4473–4476.

[18] J. Li, Y. Yu, L. Zhang, Bismuth oxyhalide nanomaterials: layered structures meet photocatalysis, Nanoscale 6 (2014) 8473–8488.

[19] H. Li, J. Shang, J. Shi, K. Zhao, L. Zhang, Facet-dependent solar ammonia synthesis of BiOCl nanosheets via a proton-assisted electron transfer pathway, Nanoscale 8 (2016) 1986–1993.

[20] H. Li, S. Chen, H. Shang, X. Wang, Z. Yang, Z. Ai, L. Zhang, Surface hydrogen bond network spatially confined BiOCl oxygen vacancy for photocatalysis, Sci. Bull. 65 (2020) 1916–1923.

[21] H. Li, J. Shang, H. Zhu, Z. Yang, Z. Ai, L. Zhang, Oxygen vacancy structure associated photocatalytic water oxidation of BiOCl, ACS Catal. 6 (2016) 8276–8285.

[22] H. Li, F. Qin, Z. Yang, X. Cui, J. Wang, L. Zhang, New reaction pathway induced by plasmon for selective benzyl alcohol oxidation on BiOCl possessing oxygen vacancies, J. Am. Chem. Soc. 139 (2017) 3513–3521.

[23] C. Mao, H. Cheng, H. Tian, H. Li, W.J. Xiao, H. Xu, J. Zhao, L. Zhang, Visible light driven selective oxidation of amines to imines with BiOCl: does oxygen vacancy concentration matter? Appl. Catal. B: Environ. 228 (2018) 87–96.

[24] H. Wang, D. Yong, S. Chen, S. Jiang, X. Zhang, W. Shao, Q. Zhang, W. Yan, B. Pan, Y. Xie, Oxygen-vacancy-mediated exciton dissociation in BiOBr for boosting charge-carrier-involved molecular oxygen activation, J. Am. Chem. Soc. 140 (2018) 1760–1766.

[25] H. Wang, X. Yang, W. Shao, S. Chen, J. Xie, X. Zhang, J. Wang, Y. Xie, Ultrathin black phosphorus nanosheets for efficient singlet oxygen generation, J. Am. Chem. Soc. 137 (2015) 11376–11382.

[26] H. Wang, S. Jiang, S. Chen, D. Li, X. Zhang, W. Shao, X. Sun, J. Xie, Z. Zhao, Q. Zhang, Y. Tian, Y. Xie, Enhanced singlet oxygen generation in oxidized graphitic carbon nitride for organic synthesis, Adv. Mater. 28 (2016) 6940–6945.

[27] H. Wang, S. Chen, D. Yong, X. Zhang, S. Li, W. Shao, X. Sun, B. Pan, Y. Xie, Giant electron-hole interactions in confined layered structures for molecular oxygen activation, J. Am. Chem. Soc. 139 (2017) 4737–4742.

[28] X. Guo, Q. Li, M. Zhang, M. Long, L. Kong, Q. Zhou, H. Shao, W. Hu, T. Wei, Enhanced photocatalytic performance of N-nitrosodimethylamine on TiO2 nanotube based on the role of singlet oxygen, Chemosphere 120 (2015) 521–526.

[29] Q. Yi, J. Ji, B. Shen, C. Dong, J. Liu, J. Zhang, M. Xing, Singlet oxygen triggered by superoxide radicals in a molybdenum cocatalytic fenton reaction with enhanced redox activity in the environment, Environ. Sci. Technol. 53 (2019) 9725–9733.

[30] Y. Qian, D. Li, Y. Han, H. Jiang, Photocatalytic molecular oxygen activation by regulating excitonic effects in covalent organic frameworks, J. Am. Chem. Soc. 142 (2020) 20763–20771.

[31] A.M. Held, D.J. Halko, J.K. Hurst, Mechanisms of chlorine oxidation of hydrogen peroxide, J. Am. Chem. Soc. 100 (1978) 5732–5740.

[32] S. Miyamoto, G.R. Martinez, A.P.B. Martins, M.H.G. Medeiros, P.D. Mascio, Direct evidence of singlet molecular oxygen [O2 (1Δg)] production in the reaction of linoleic acid hydroperoxide with peroxynitrite, J. Am. Chem. Soc. 125 (2003) 4510–4517.

[33] S. Miyamoto, G.E. Ronsein, F.M. Prado, M. Uemi, T.C. Correa, I.N. Toma, A. Bertolucci, M.C. Oliveira, F.D. Motta, M.H. Medeiros, P.D. Mascio, Biological hydroperoxides and singlet molecular oxygen generation, IUBMB Life 59 (2007) 322–331.

[34] S. Miyamoto, P. Di Mascio, Lipid hydroperoxides as a source of singlet molecular oxygen, Subcell. Biochem 77 (2014) 3–20.

[35] X. Lu, W. Qiu, J. Ma, H. Xu, D. Wang, H. Cheng, W. Zhang, X. He, The overestimated role of singlet oxygen for pollutants degradation in some non-photochemical systems, Chem. Eng. J. 401 (2020), 126128.

[36] Y. Zong, Y. Shao, Y. Zeng, B. Shao, L. Xu, Z. Zhao, W. Liu, D. Wu, Enhanced oxidation of organic contaminants by iron(II)-activated periodate: the significance of high-valent iron-oxo species, Environ. Sci. Technol. 55 (2021) 7634–7642.

[37] H. Zhao, X. Liu, Y. Dong, Y. Xia, H. Wang, X. Zhu, Fabrication of a Z-scheme {001}/{110} facet heterojunction in BiOCl to promote spatial charge separation, ACS Appled Mater. Interfaces 12 (2020) 31532–31541.

[38] Y. Shiraishi, M. Hashimoto, K. Chishiro, K. Moriyama, S. Tanaka, T. Hirai, Photocatalytic dinitrogen fixation with water on bismuth oxychloride in chloride solutions for solar-to-chemical energy conversion, J. Am. Chem. Soc. 142 (2020) 7574–7583.

[39] H. Wang, Z. Han, Y. Zhou, X. Liu, D. Zeng, W. Wang, D. Sarker, L. Zhang, W. Wang, Efficient photocatalytic chlorine production on bismuth oxychloride in chloride solution, Appl. Catal. B: Environ. 297 (2021), 120436.

[40] Y. Zhou, H. Wang, X. Liu, D. Zeng, K. Wang, L. Zhang, W. Wang, An efficient strategy for selective oxidation of ammonia nitrogen into N2 over BiOCl photocatalyst, Appl. Catal. B: Environ. 294 (2021), 120265.

[41] C.W. Jefford, The photo-oxygenation of olefins and the role of zwitterionic peroxides, Chem. Soc. Rev. (1993) 59–66.

[42] P.R. Tentscher, M. Bourgin, U. von Gunten, Ozonation of para-substituted phenolic compounds yields p-Benzoquinones, other cyclic alpha,beta-unsaturated ketones, and substituted catechols, Environ. Sci. Technol. 52 (2018) 4763–4773.

[43] P. Di Mascio, G.R. Martinez, S. Miyamoto, G.E. Ronsein, M.H.G. Medeiros, J. Cadet, Singlet molecular oxygen reactions with nucleic acids, lipids, and proteins, Chem. Rev. 119 (2019) 2043–2086.

[44] Z. Li, Y. Luan, Y. Qu, L. Jing, Modification strategies with inorganic acids for efficient photocatalyst by promoting the adsorption of O2, ACS Appl. Mater. Interfaces 7 (2015) 22727–22740.

[45] S. Chen, R. Yan, X. Zhang, K. Hu, Z. Li, M. Humayun, Y. Qu, L. Jing, Photogenerated electron modulation to dominantly induce efficient 2,4-dichloro-phenol degradation on BiOBr nanoplates with different phosphate modification, Appl. Catal. B: Environ. 209 (2017) 320–328.

[46] H. Wang, X. Sun, D. Li, X. Zhang, S. Chen, W. Shao, Y. Tian, Y. Xie, Boosting hot-electron generation: exciton dissociation at the order-disorder interfaces in polymeric photocatalysts, J. Am. Chem. Soc. 139 (2017) 2468–2473.

[47] X. Sun, X. Luo, X. Zhang, J. Xie, S. Jin, H. Wang, X. Zheng, X. Wu, Y. Xie, Enhanced superoxide generation on defective surfaces for selective photooxidation, J. Am. Chem. Soc. 141 (2019) 3797–3801.

[48] X. Guo, Q. Li, M. Zhang, M. Long, L. Kong, Q. Zhou, H. Shao, W. Hu, T. Wei, Enhanced photocatalytic performance of N-nitrosodimethylamine on TiO2 nanotube based on the role of singlet oxygen, Chemosphere 120 (2015) 521–526.

[49] Y. Bu, H. Li, W. Yu, Y. Pan, L. Li, Y. Wang, L. Pu, J. Ding, G. Gao, B. Pan, Peroxydisulfate activation and singlet oxygen generation by oxygen vacancy for degradation of contaminant, Environ. Sci. Technol. 55 (2021) 2110–2120.

[50] T. Li, Y. Jiang, X. An, H. Liu, C. Hu, J. Qu, Transformation of humic acid and halogenated byproduct formation in UV-chlorine processes, Water Res. 102 (2016) 421–427.

[51] R. Song, H. Wang, M. Zhang, Y. Liu, X. Meng, S. Zhai, C. Wang, T. Gong, Y. Wu, X. Jiang, W. Bu, Near-infrared light-triggered chlorine radical (•Cl) stress for cancer therapy, Angew. Chem. Int. Ed. 59 (2020) 21032–21040.

[52] Q. Huang, M. Cao, Z. Ai, L. Zhang, Reactive oxygen species dependent degradation pathway of 4-chlorophenol with Fe@Fe2O3 core–shell nanowires, Appl. Catal. B: Environ. 162 (2015) 319–326.

[53] P. Chen, Q. Zhang, X. Zheng, C. Tan, M. Zhuo, T. Chen, F. Wang, H. Liu, Y. Liu, Y. Feng, W. Lv, G. Liu, Phosphate-modified m-Bi2O4 enhances the absorption and photocatalytic activities of sulfonamide: Mechanism, reactive species, and reactive sites, J. Hazard. Mater. 384 (2020), 121443.

[54] N. Sun, Y. Qu, C. Yang, Z. Yang, R. Yan, W. E, Z. Zhang, Z. Li, H. Li, I. Khan, R. Sun, L. Jing, H. Fu, Efficiently photocatalytic degradation of monochlorophenol on in-situ fabricated BiPO4/β-Bi2O3 heterojunction microspheres and O2 free hole-induced selective dechloridation conversion with H2 evolution, Appl. Catal. B: Environ. 263 (2020), 118313.

[55] Z. Zeng, Y. Fan, X. Quan, H. Yu, S. Chen, S. Zhang, Energy transfer mediated oxygen activation in carbonyl functionalized carbon nitride nanosheets for high-efficient photocatalytic water disinfection and organic pollutants degradation, Water Res. 177 (2020), 115798.